Journal of Physics:
Conference Series

PURPOSE-LED
PUBLISHING™

PAPER • **OPEN ACCESS**

Near–Field Crack Localization using Spectral Estimation Methods

To cite this article: Ahmed Desoki *et al* 2025 *J. Phys.: Conf. Ser.* **3070** 012003

ASAT-21 IOP Publishing
Journal of Physics: Conference Series **3070** (2025) 012003 doi:10.1088/1742-6596/3070/1/012003

Near–Field Crack Localization using Spectral Estimation Methods

Ahmed Desoki[1*], **Mohamed Mahgoub**[1] **and Hani Negm**[1]

[1]Aerospace Engineering Department, Cairo University, 12613, Giza, Egypt

E-mail: ahmed.desoki@cu.edu.eg

Abstract. Non–Destructive Inspection (NDI) using phased arrays is used to detect defects in structures of Aerospace vehicles, such as cracks, corrosion spots, composite material delaminations and others. Ultrasonic Imaging, an advanced NDI technique, relies on advanced signal processing methods to accurately localize defects. The Multiple Signal Classification (MUSIC) is a high resolution spectral estimation method typically used for Angle of Arrival (AOA) estimation. This work examines the applicability and performance of the MUSIC method for localization, rather than AOA estimation, of point defects and finite–length cracks in structures. The advantages of MUSIC over traditional methods like the Delay and Sum Beamformer (DSBF) are highlighted.

1 Introduction

The aviation industry is one of the most safety-critical sectors, where minor structural defects can lead to catastrophic failures. The integrity of the aircraft structure is essential to ensure the safety of crew and aircraft. Structural defects such as cracks, corrosion, and delamination, if undetected, can propagate over time and ultimately lead to catastrophic failures [1]. Early detection of these defects is a critical research focus, particularly in the aerospace industry, where plate-like structures require thorough inspection. Early detection not only ensures high levels of operational safety but also extends the service life of these structures. Consequently, the implementation of reliable inspection methods during both manufacturing and in–service operations is essential to prevent catastrophic failures [2]. Non–Destructive Inspection (NDI) serves as a pivotal solution to achieve these objectives.

NDI is widely utilized in many industrial fields such as aerospace, oil and gas, power generation, transportation, and medical diagnostics. Common NDI methods include Visual Inspection, Liquid Penetrant Testing (LPT), Magnetic Particle Testing (MPT), Eddy Current Testing (ECT), Radiographic Testing (RT), and Ultrasonic Testing (UT) [3]. Among these methods, Ultrasonic Imaging (UI) stands out as one of the most advanced and reliable NDI techniques. UI offers several advantages, including the ability to detect both internal and surface defects, safe for human operators as it does not emit ionizing radiation, high sensitivity, a long detection range, testing speed, ease, and instantaneous printable results [4, 5, 6].

A critical aspect of UI is the application of signal processing methods to translate the measured signals into images that reveal defect locations [7]. There are several methods that can estimate the Angle of Arrival (AOA) of received signals. Typical example is the well–known Delay and Sum Beamformer (DSBF). In this paper, It is demonstrated that AOA estimation using DSBF reduces to the periodogram non–parametric spectral estimation method [8, 9]. The Multiple Signal Classification (MUSIC) is another spectral estimation method known for its super resolution. In this work, the DSBF and MUSIC spectral estimation methods are both formulated for estimating the location (range r and AOA θ) of a Near–Field (NF) source. Their performance is examined in a great details. The performance of these methods for structural defect detection is examined in detail.

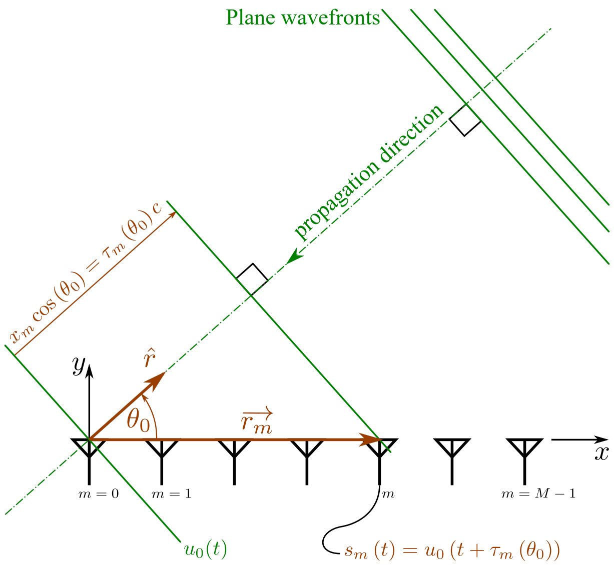

Figure 1: Signal model

2 FF AOA Estimation using DSBF

As shown in figure 1, for a signal coming from a Far–field (FF) source at an Angle of Arrival (AOA) θ_0, the signal received at the m–th sensor of a sensor array can be written as

$$s_m(t) = u_0(t + \tau_m(\theta_0)) \tag{1}$$

where $u_0(t)$ is the signal arriving at the origin

$$\tau_m(\theta) \equiv \frac{x_m \cos(\theta)}{c} \tag{2}$$

and c is the propagation speed.

For an array of M receivers, the Delay and Sum BeamFormer (DSBF) steers the array output at an angle θ as [10]

$$y(t,\theta) = \sum_{m=0}^{M-1} s_m(t - \tau_m(\theta)) \tag{3}$$

When θ coincides with the true source angle θ_0, the summation in equation (3) yields constructive interference [10]. Equation (3) can be implemented in the temporal frequency domain as [9]

$$Y(\omega,\theta) = \sum_{m=0}^{M-1} S_m(\omega)\, e^{-j\omega\tau_m(\theta)} \tag{4}$$

where

$$S_m(\omega) \equiv \mathcal{F}_t[s_m(t)] \tag{5}$$

is the temporal Fourier Transform (FT) of $s_m(t)$. Substituting equation (2) in (4) yields

$$\begin{align} Y(\omega,\theta) &= \sum_{m=0}^{M-1} S_m(\omega)\, e^{-j\frac{\omega}{c}x_m\cos(\theta)} \tag{6} \\ &= \sum_{m=0}^{M-1} S_m(\omega)\, e^{-jkx_m\cos(\theta)} \tag{7} \end{align}$$

where

$$k \equiv \frac{\omega}{c} \tag{8}$$

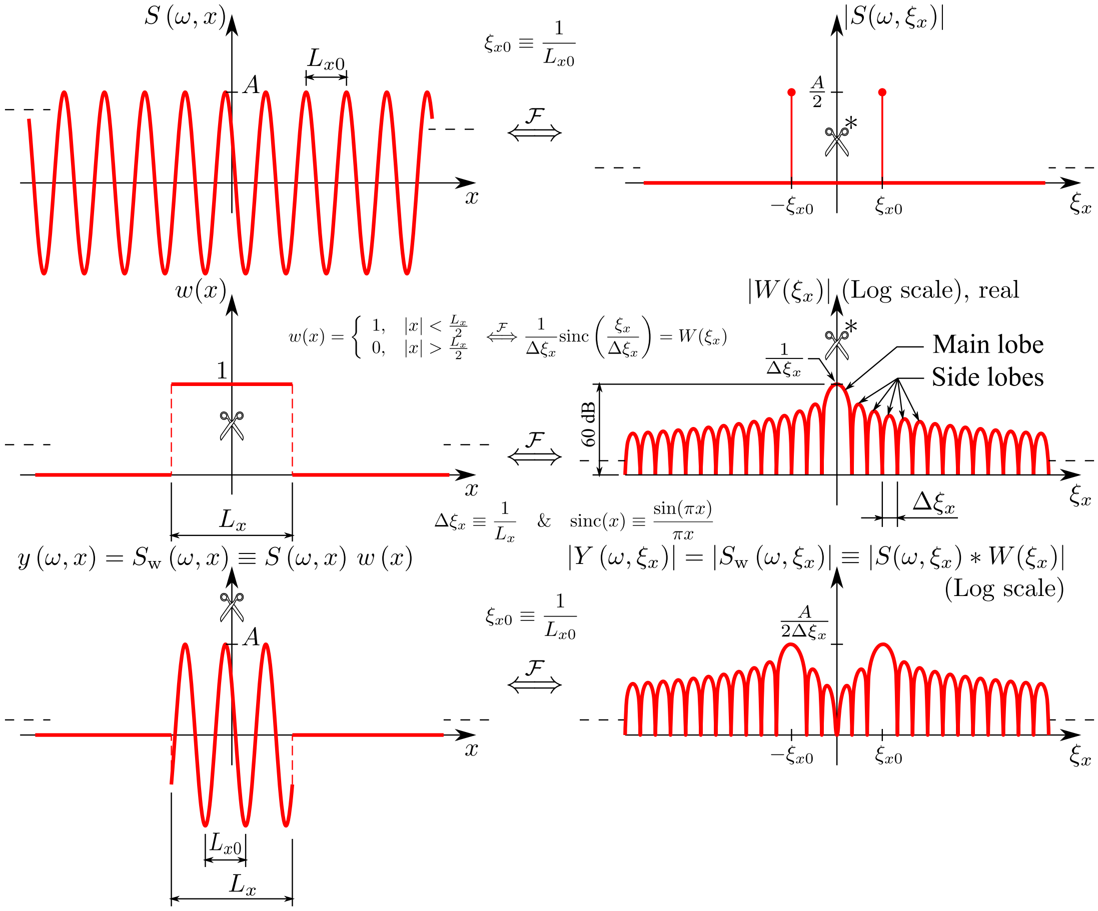

Figure 2: Illustration of the SXFT, or BF using a (fictitious) linear aperture

$$= \frac{2\pi}{\lambda} \tag{9}$$

is the spatial frequency (also known as "wave–number").

By defining

$$k_x \equiv k \cos(\theta) \tag{10}$$

equation (7) is written as

$$Y(\omega, k_x) = \sum_{m=0}^{M-1} S_m(\omega)\, e^{-jk_x x_m} \tag{11}$$

Similar to the temporal Short–Time Fourier Transform (STFT) [8], the spatial Short x Fourier Transform (SXFT) can be written as

$$S_{\text{w}}(k_x) = \int_{-L_x/2}^{L_x/2} s_{\text{w}}(x)\ e^{-jk_x x} dx \tag{12}$$

By comparing equations (12) and (11), it is clear that $Y(\omega, k_x)$ is the SXFT of $S(\omega, x)$ over a finite–width fictitious line aperture spanning $x_m \in [-L_x/2, L_x/2]$. That is

$$\begin{align} Y(\omega, k_x) &= \text{SXFT}[S(\omega, x)] \tag{13} \\ &= \text{SXFT}[\mathcal{F}_t[s(t, x)]] \tag{14} \end{align}$$

This is illustrated in figure 2.

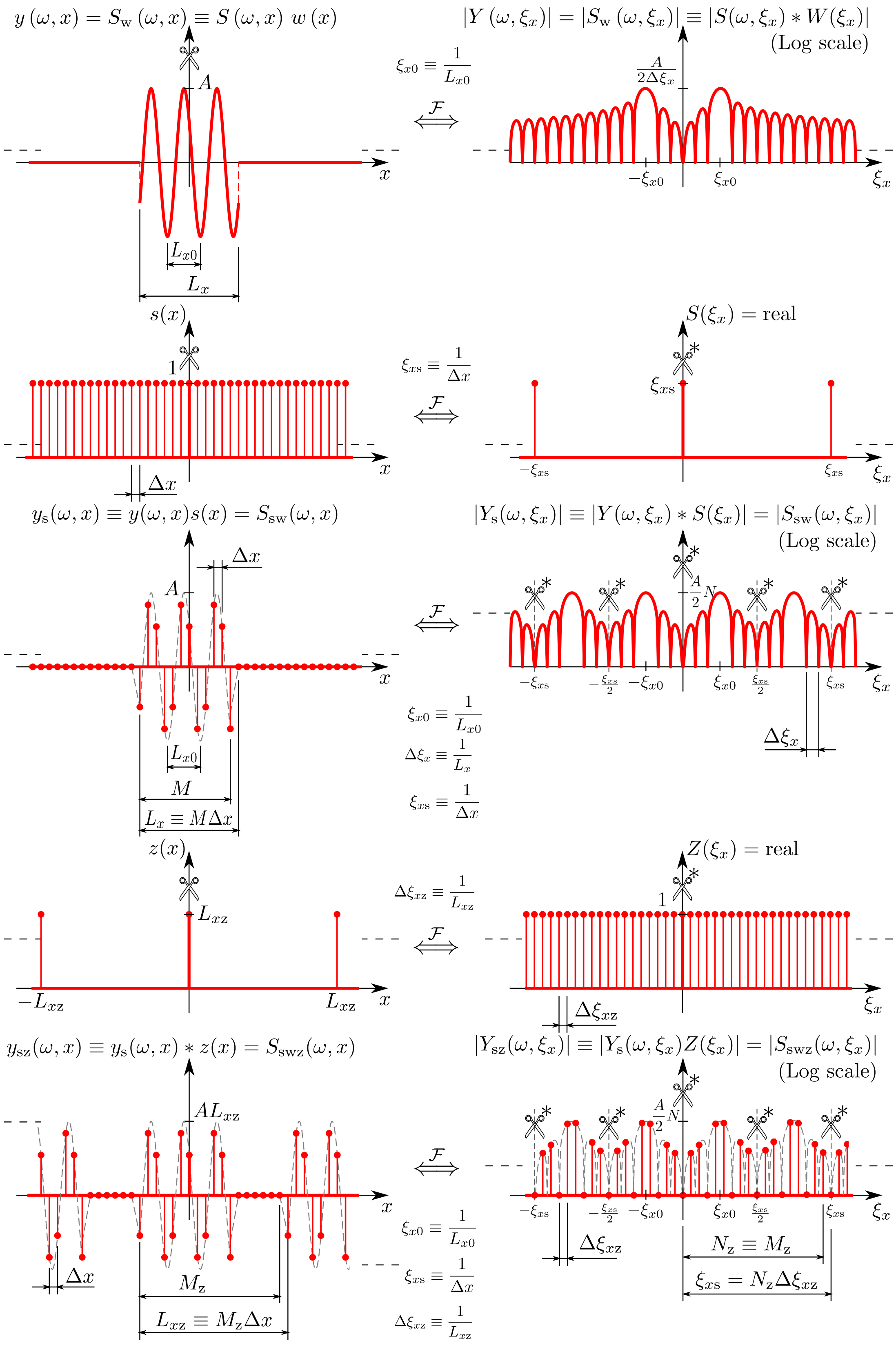

Figure 3: Digital calculation of the DXSXFT by the zero–padded DFT

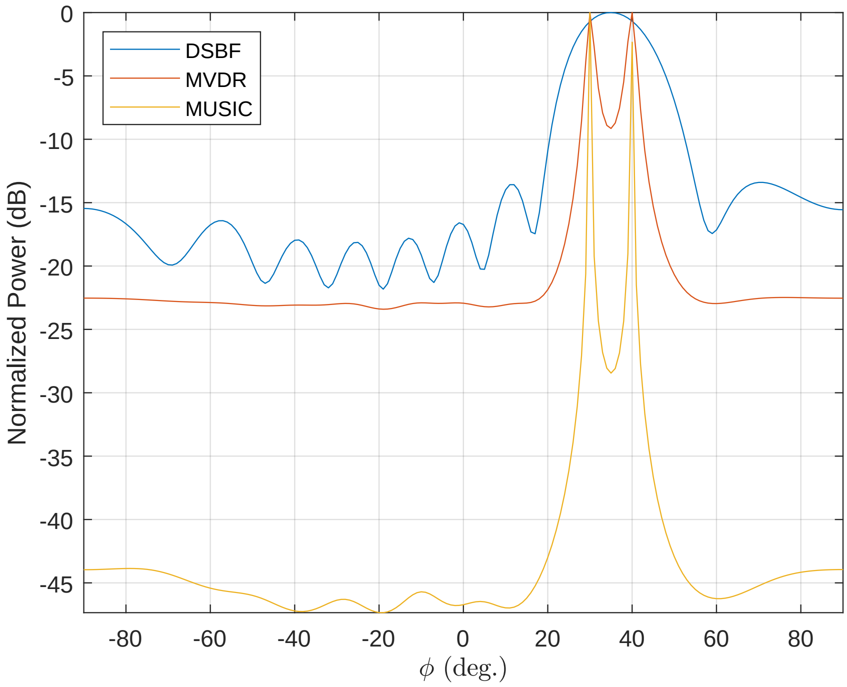

Figure 4: Several spectral estimation methods detecting AOA's of FF sources at $\phi = 30°$ and $40°$

k_x can be mapped back to the source AOA as [equations (10) and (9)]

$$\theta = \cos^{-1}\left(\frac{k_x}{k}\right) \tag{15}$$

$$= \cos^{-1}\left(\frac{\xi_x}{\xi}\right) \tag{16}$$

$$\xi \equiv \frac{1}{\lambda} \tag{17}$$

$$\phi \equiv 90° - \theta \tag{18}$$

$$= \sin^{-1}\left(\frac{\xi_x}{\xi}\right) \tag{19}$$

Using a Uniform Linear Array (ULA), the SXFT of equation (14) is discretized with $\Delta x \equiv \frac{L_x}{M}$ to obtain the Discrete x Short x Fourier Transform (DXSXFT) [8]

$$Y_\mathrm{s}\left(\omega, k_x\right) = \mathrm{DXSXFT}\left[\mathcal{F}_t\left[s\left(t, x, y\right)\right]\right] \tag{20}$$

as graphically illustrated in figure 3. Finally, the DXSXFT is digitally calculated by applying the zero–padded Discrete Fourier Transform (DFT) [8] to obtain Y_sz, as graphically illustrated in figure 3.

In the presence of measurement noise, estimating the magnitude $|Y_\mathrm{s}|$ is a standard spectral estimation problem [9]. The DSBF is in fact the periodogram non–parametric spectral estimation method [8, 9]

$$R_{YY} = \left|Y_\mathrm{sz}\right|^2 \tag{21}$$

There are several spectral estimation methods other than the periodogram method [9]. Figure 4 compares spectral estimation using DSBF with the famous Capon's Minimum Variance Distortionless Response (MVDR) beamformer and the MUltiple SIgnal Classification (MUSIC) methods. As shown in the figure, in case of multiple source signals, the contribution from one source biases the DSBF estimator output along other directions of arrivals [11]. If there are two sources located inside the the main lobe, their peaks merge forming a single peak, deteriorating the resolution. On the other hand, the MUSIC method has significantly higher resolution that can resolve arbitrary closely signal sources [10].

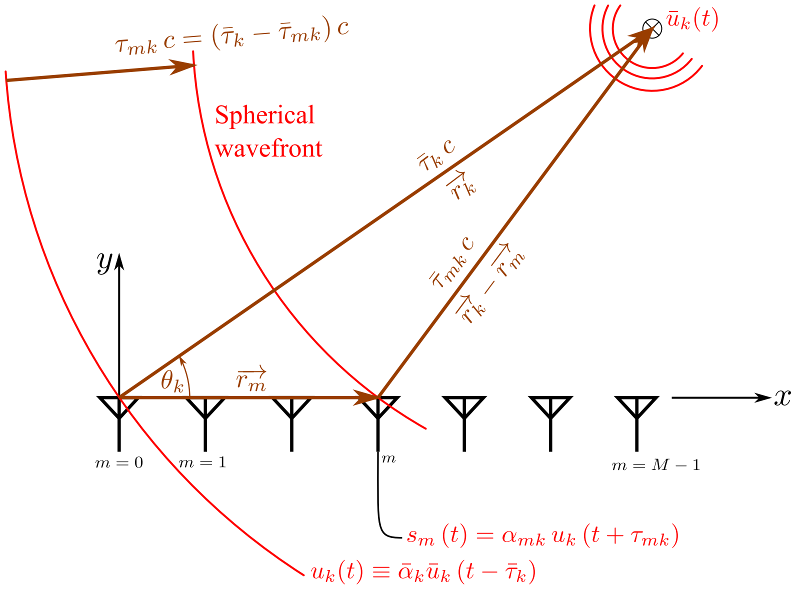

Figure 5: NF signal model

3 NF Defect Localization using Spectral Estimation Methods

It was shown in the previous section that any spectral estimation method can be systematically applied to the estimate the AOA of a FF source. In this section, the DSBF and MUSIC spectral estimation methods are formulated for estimating the location (range r and AOA θ) of a Near–Field (NF) source.

3.1 NF DSBF

As shown in figure 5, for a NF source located at $\overrightarrow{r_k}$, the signal received at the m–th sensor can be written as

$$s_m(t) = \alpha_{mk} u_k(t + \tau_{mk}) \tag{22}$$

where

$$\begin{aligned} \tau_{mk} &\equiv \tau_m(\overrightarrow{r_k}) && (23)\\ &\equiv \bar{\tau}_k - \bar{\tau}_{mk} && (24)\\ \bar{\tau}_k &\equiv \bar{\tau}(\overrightarrow{r_k}) && (25)\\ \bar{\tau}_{mk} &\equiv \bar{\tau}_m(\overrightarrow{r_k}) && (26) \end{aligned}$$

$$\begin{aligned} \alpha_{mk} &\equiv \alpha_m(\overrightarrow{r_k}) && (27)\\ &\equiv \frac{\bar{\alpha}_{mk}}{\bar{\alpha}_k} && (28)\\ \bar{\alpha}_k &\equiv \bar{\alpha}(\overrightarrow{r_k}) && (29)\\ \bar{\alpha}_{mk} &\equiv \bar{\alpha}_m(\overrightarrow{r_k}) && (30) \end{aligned}$$

and

$$\bar{\alpha}_m(\vec{r}) = \frac{1}{|\overrightarrow{r_m} - \vec{r}|} \tag{31}$$

represents the attenuation in the source signal amplitude due to wave propagation spread in a plate.

Similar to equation (4), the NF DSBF in the temporal frequency domain becomes

$$Y(\omega, \overrightarrow{r_k}) = \sum_{m=0}^{M-1} S_m(\omega)\, e^{-j\omega\tau_{mk}} \tag{32}$$

3.2 NF MUSIC

For a set of K sources and in the presence of arbitrary noise, the received signal at the m–th sensor can be written as

$$s_m(t) = \sum_{k=1}^{K} \alpha_{mk} u_k(t + \tau_{mk}) + n_m(t) \tag{33}$$

Equation (33) can be written in the frequency–domain as

$$S_m(\omega) = \sum_{k=1}^{K} \alpha_{mk} U_k(\omega) e^{j\omega\tau_{mk}} + N_m(\omega) \tag{34}$$

or in vector form

$$\{S(\omega)\}_{M\times 1} = [A]_{M\times K} \{U(\omega)\}_{K\times 1} + \{N(\omega)\}_{M\times 1} \tag{35}$$

where

$$\{S(\omega)\} \equiv \left\{ \begin{array}{c} S_0(\omega) \\ S_1(\omega) \\ \vdots \\ s_{M-1}(\omega) \end{array} \right\}_{M\times 1} \tag{36}$$

$$[A]_{M\times K} \equiv [\{a_1\}, \{a_2\}, \ldots, \{a_K\}] \tag{37}$$

$$\{a_k\}_{M\times 1} = \left\{ \begin{array}{c} \alpha_{0k} e^{j\omega\tau_{0k}} \\ \alpha_{1k} e^{j\omega\tau_{1k}} \\ \vdots \\ \alpha_{(M-1)k} e^{j\omega\tau_{(M-1)k}} \end{array} \right\} \tag{38}$$

$$\{U(\omega)\}_{K\times 1} = \left\{ \begin{array}{c} U_1(\omega) \\ U_2(\omega) \\ \vdots \\ U_K(\omega) \end{array} \right\} \tag{39}$$

By defining the array output auto–spectrum matrix

$$[R_{SS}(\omega)] \equiv \underset{\text{ensemble}}{E\left[\left[\{S(\omega)\}\{S(\omega)\}^{\dagger}\right]_{M\times M}\right]} \tag{40}$$

and assuming the noise signals are uncorrelated among themselves and with source signals yields

$$\begin{aligned} [R_{SS}]_{M\times M} &= [A]_{M\times K}\, E\left[\{U(\omega)\}_{K\times 1} \{U(\omega)\}^{\dagger}_{1\times K}\right] [A]^{\dagger}_{K\times M} + \left\lceil \operatorname{diag}\left(\sigma^2\right) \right\rfloor_{M\times M} && (41) \\ &= [A]_{M\times K} [R_{UU}]_{K\times K} [A]^{\dagger}_{K\times M} + \left\lceil \operatorname{diag}\left(\sigma^2\right) \right\rfloor_{M\times M} && (42) \\ &= \overline{[R_{SS}]}_{M\times M} + \left\lceil \operatorname{diag}\left(\sigma^2\right) \right\rfloor_{M\times M} && (43) \end{aligned}$$

where $[R_{UU}]_{K\times K}$ is the sources auto–spectrum matrix,

$$\overline{[R_{SS}]}_{M\times M} = [A]_{M\times K} [R_{UU}]_{K\times K} [A]^{\dagger}_{K\times M} \tag{44}$$

is the noise free sensors auto–spectrum matrix,

$$\left\lceil \operatorname{diag}\left(\sigma^2\right) \right\rfloor = \begin{bmatrix} \sigma_0^2 & 0 & \cdots & 0 \\ 0 & \sigma_1^2 & \cdots & 0 \\ \vdots & \vdots & \ddots & \vdots \\ 0 & 0 & \cdots & \sigma_{M-1}^2 \end{bmatrix}_{M\times M} \tag{45}$$

and σ_m^2 is the noise power at the m–th sensor.

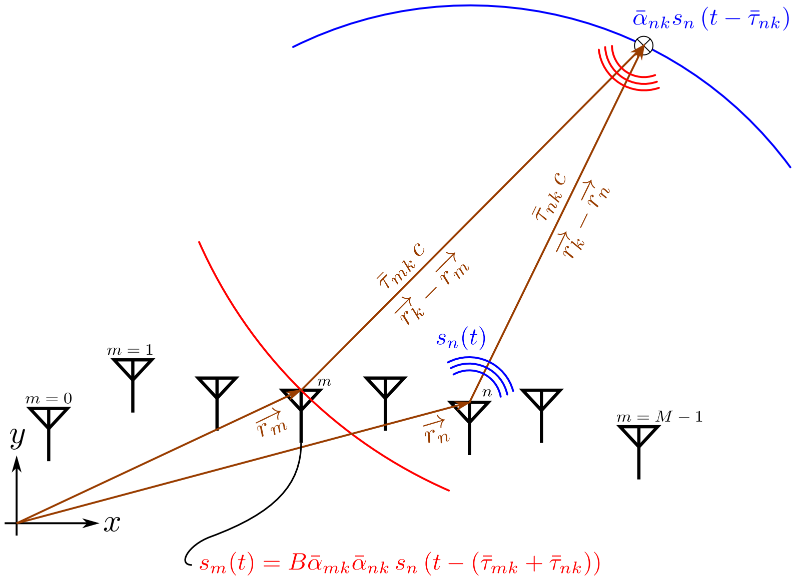

Figure 6: Signal transmission and reception model

If the K source signals are uncorrelated, then the $[R_{UU}]_{K\times K}$ matrix will have full rank. Otherwise, it will have a rank equal to the number of uncorrelated signals. By definition [equation (40)] $[R_{SS}(\omega)]$ is Hermitian and always non–negative definite. Assuming uncorrelated source signals, $[R_{UU}]_{K\times K}$ is full rank. Hence, eigenvalues of the positive definite auto–spectrum matrix $[R_{UU}]_{K\times K}$ are all positive $\mu_1 \geqslant \mu_2 \geqslant \ldots \geqslant \mu_K > 0$ [10]. Thus, eigenvalues of $\overline{[R_{SS}]}$ are denoted as [10]

$$\overline{\lambda}_m = \begin{cases} \mu_{k=m} & m = 1, 2, \ldots, K \\ \\ 0 & m = K+1, \ldots, M \end{cases} \tag{46}$$

Then for the ideal model described by equation (41), eigenvalue decomposition of $[R_{SS}]$ yields the M eigenvalues

$$\lambda_m = \begin{cases} \mu_{k=m} + \sigma_{\mathrm{m}}^2 & m = 1, 2, \ldots, K \\ \\ \sigma_{\mathrm{m}}^2 & m = K+1, \ldots, M \end{cases} \tag{47}$$

and their associated eigenvectors $\{\beta_1\}, \{\beta_2\}, \ldots, \{\beta_K\}, \{\beta_{K+1}\}, \ldots, \{\beta_M\}$. Based on these assumptions, peaks of the function

$$P_{\mathrm{MUSIC}}\left(\overrightarrow{r_k}\right) = \frac{1}{\left\{a\left(\overrightarrow{r_k}\right)\right\}^{\dagger} [B_{\mathrm{n}}] [B_{\mathrm{n}}]^{\dagger} \left\{a\left(\overrightarrow{r_k}\right)\right\}} \tag{48}$$

will correspond to the true positions, where $[B_{\mathrm{n}}]$ is the matrix whose columns are the eigenvectors associated with the noise eigenvalues

$$[B_{\mathrm{n}}] = \left[\{\beta_{K+1}\}, \ldots, \{\beta_M\}\right] \tag{49}$$

4 Simulation Methodology

As shown in figure 6, the n–th element of the array transceivers transmits a signal $s_n(t)$. This signal propagates omni–directionally till it is reflected at a defect located at $\overrightarrow{r_k}$, back to the sensor array. The m–th sensor thus receives

$$s_m(t) = B\bar{\alpha}_{mk}\bar{\alpha}_{nk} s_n\left(t - \left(\bar{\tau}_{mk} + \bar{\tau}_{nk}\right)\right) \tag{50}$$

where B represents the relative reflection attenuation at the defect.

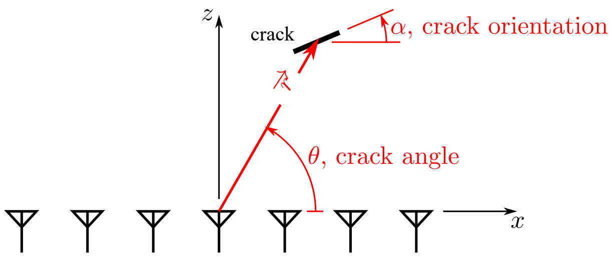

Figure 7: Coordinate system and crack configurations

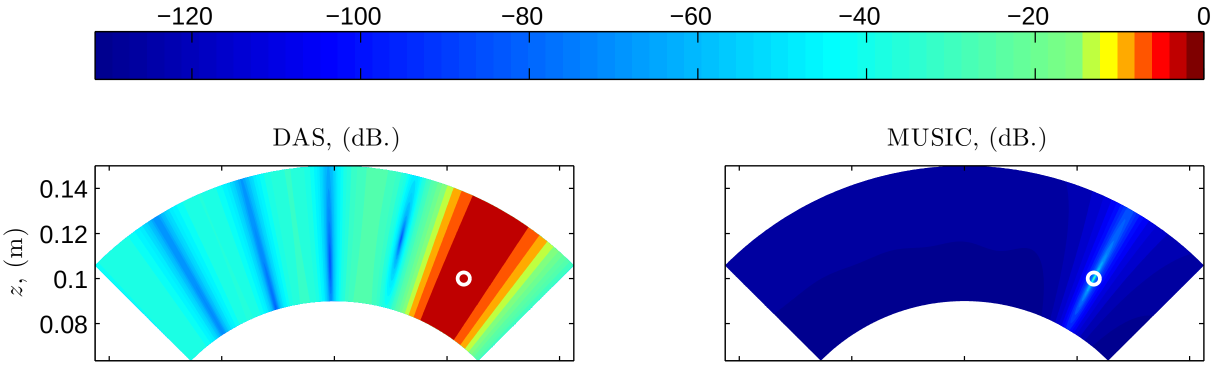

Figure 8: Point defect at $\theta = 60^\circ + \frac{\Delta\theta}{2}$ (best case of a point defect where a grid point coincides with the point defect) DSBF (left), and MUSIC (right)

5 Simulation and Results

A MATLAB code was built to implement equation (50), with $B = 0.05$, and the NF DSBF and MUSIC methods explained in sec. 3. The test configurations of [12] are used. That is, Hann smoothed tone–burst excitation signal having three cycles of $f_c = 300$ kHz are used. This signal is initially transmitted from the 1st element of the sensor array so that it is reflected at the defects and returns back to the array sensors. For a 1 mm thick Aluminum alloy plate, the wave propagation speed in 5440 m/s. A ULA having $M = 8$ and sensor spacing $d = 8$ mm is used. The sampling frequency is set to $f_s = 4f_c$. Contrary to [12], Additive White Gaussian Noise (AWGN) is added to the received signals so that the Signal–to–Noise Ratio (SNR) is $\mathrm{SNR} = 1$. $N = 2048$ time samples were used to estimate the auto–spectrum matrix [10]. The origin of the $x - z$ coordinate system is set at the sensor array center, as shown in figure 7. The simulated defect/crack is set at $z = 100$ mm and $\theta = 60^\circ$, unless otherwise specified. The results of MUSIC method are compared to those of the conventional DSBF.

To demonstrate the high resolution of MUSIC, a very fine calculation grid with $\Delta\theta = 0.25^\circ$ and 100 radial steps is used for the B–scan image. The grid spans the range $\theta = [45^\circ - \frac{\Delta\theta}{2}, 135^\circ + \frac{\Delta\theta}{2}]$ and $r = [90\,\mathrm{mm}, 150\,\mathrm{mm}]$. The angular grid span is shifted by $\frac{\Delta\theta}{2}$ in order to prevent grid points from coinciding with cracks located at integer values of θ. This yields practical results, as explained later in the following section.

5.1 Point Defect

A point defect is simulated at $\theta = 60^\circ + \frac{\Delta\theta}{2}$ so that it coincides with one of the calculation grid points [7]. As shown in figure 8, MUSIC detects the defect location (AOA and radius (range)) with exceptional resolution. On the other hand, DSBF could only detect the AOA rather than the range. For the practical case where the point defect does not coincide with a grid point, $\theta = 60^\circ$, the results of figure 9(a) are obtained. This figure shows that MUSIC still yields much higher localization resolution as compared with DSBF, which fails to detect the range. In fact, for all the subsequent results, the DSBF fails to detect the defect range.

5.2 Finite–Length Crack

So far, we modeled the crack as a point. Real cracks however have finite lengths. To simulate a finite–length crack, 100 adjacent points spanning the crack length are used. The simulated cracks lengths are $\lambda/4$ long and are oriented normal to the crack position vector, unless otherwise specified.

The B–scan images calculated using both NF MUSIC and DSBF are shown in figure 9(b). As shown in the figure, the MUSIC resolution is superior to DSBF.

5.3 Factors Affecting the Detection

To further analyze the MUSIC method, the effects of crack angle, orientation, size, and SNR are discussed.

5.3.1 Crack Angular position The crack may exist at any arbitrary position. For three cracks are assumed at angles $\theta = 90°, 75° \,\&\, 60°$, the B–scan images of figures 9(b)–9(d) are calculated. As shown in the figure, MUSIC could detect cracks at all angular positions with superior resolution as compared to DSBF.

5.3.2 Crack Orientation For the same crack of figure 9(b), several crack orientation angles [figure 7] are studied and their resulting images are displayed in figure 10. As the figure shows, as the crack orientation angle deviates away from the normal to, or the coincident with, the crack position vector [figure 7], the resolution (especially the range) deteriorates considerably. This conforms with the analysis in [13].

5.3.3 Crack Size In this section, several crack lengths are analyzed as shown in figure 11. As noticed from the figure, the crack's range is correctly detected for crack sizes smaller than the signal wavelength λ. As the crack length exceeds the wavelength, the range resolution deteriorates, while the AOA resolution remains satisfactory. This suggests an upper limit for the crack size that is accurately detectable for a typical signal frequency.

Additionally, it is noticed that the AOA resolution is linearly proportional to the crack size. That is, an empirical relation can be obtained to calculate the crack size from the calculated AOA resolution.

5.3.4 Signal–to–Noise Ratio (SNR) In this section, the effect of the SNR, of the AWGN, on the proposed method is examined. Doing so, AOA is estimated for several SNR values, as shown in figure 12. As the figure shows, MUSIC resolution hardly changes with changing the SNR. This is explained due to the high number of time samples used in simulations, $N = 2048$ [14]. Figure 12 shows that the resulting high averaging could diminish the noise for the studied SNR cases, and hence all the cases are all nearly the same.

To verify this reasoning, the amount of averaging is reduced by reducing the number of time samples down to $N = 16$, to obtain the results of figure 13. For SNR as low as 0.1, 13(a) shows that MUSIC could correctly detect the AOA, rather than the range. This is however still better than the best possible DSBF results shown in figure 13(e). For higher SNR's, figures 13(b) to 13(d) show that MUSIC could accurately localize the crack with resolutions enhancing proportionally with the SNR. Further studies of the SNR effects can be found in [15, 9].

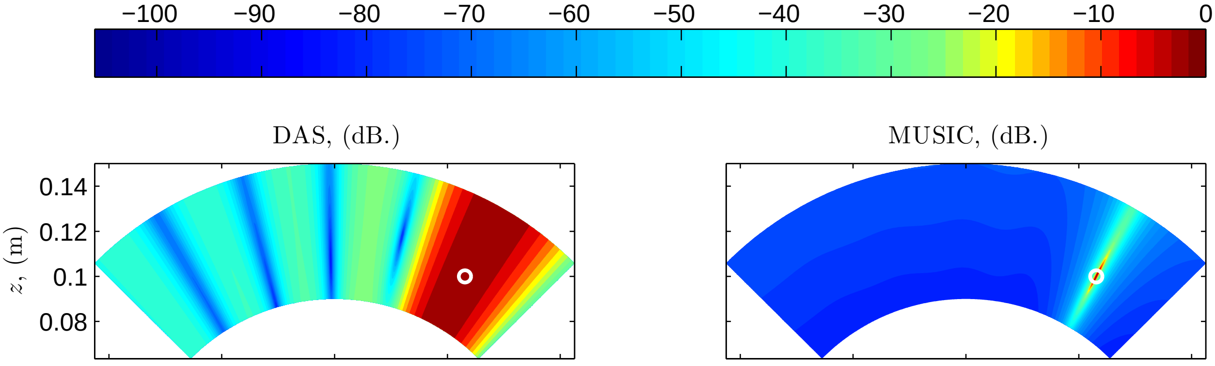

(a) Point defect at $\theta = 60°$ (normal case of a point defect where grid points surround the point defect)

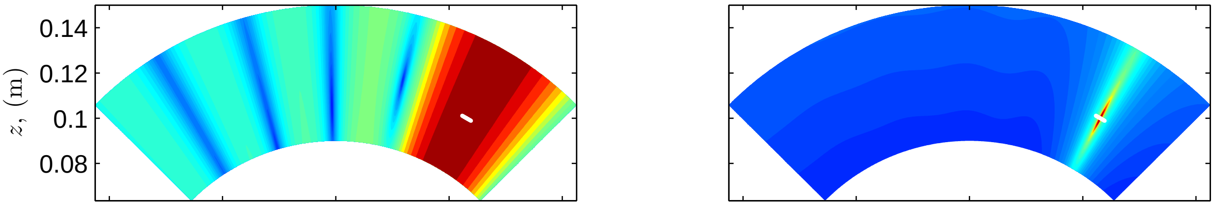

(b) One crack at $\theta = 60°$

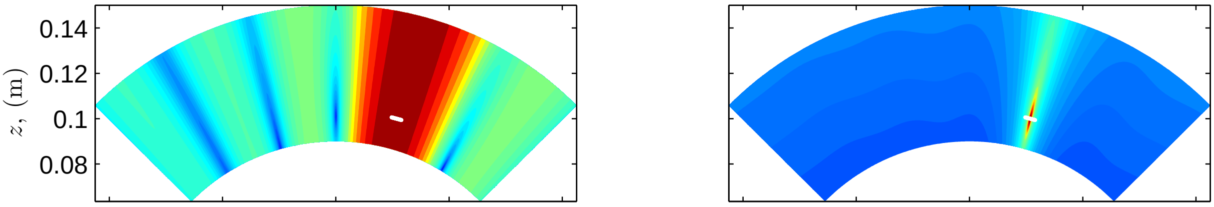

(c) One crack at $\theta = 75°$

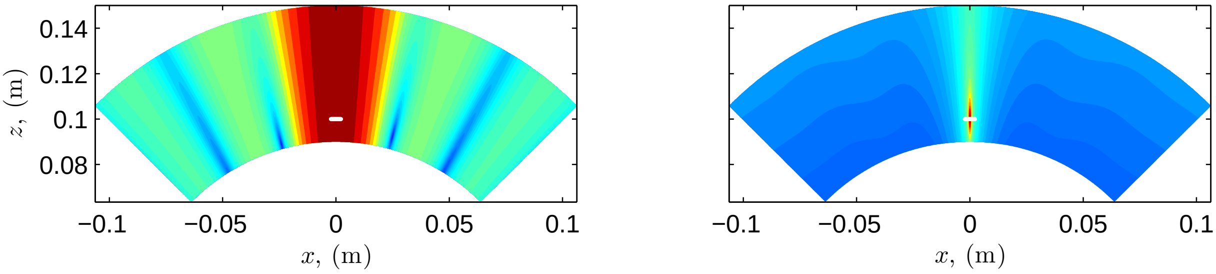

(d) One crack at $\theta = 90°$

Figure 9: (left) DSBF, and (right) MUSIC; 9(a) Point defect, (9(b)–9(d)) finite–length cracks at various angular positions

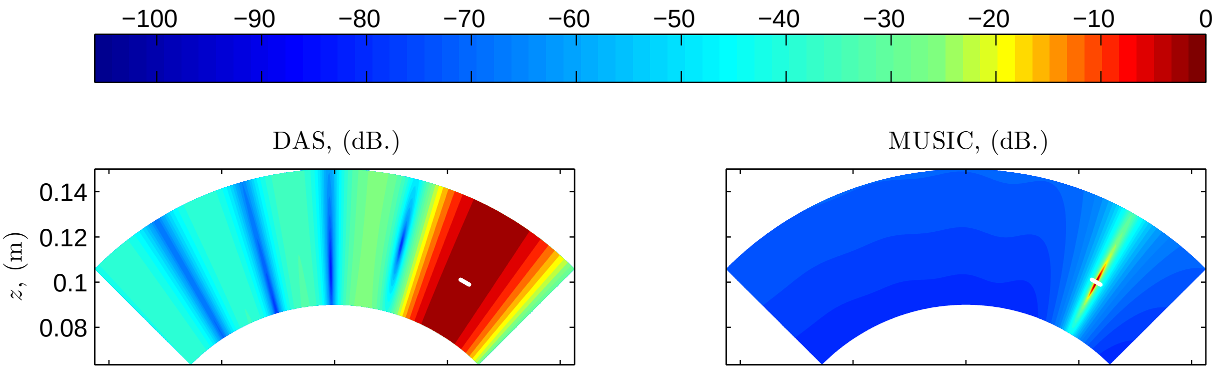

(a) $\alpha = -30°$ (normal to the crack position vector); *identical to figure 9(b)*

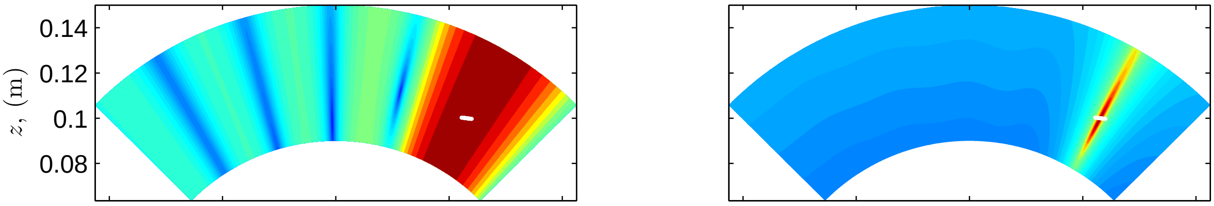

(b) $\alpha = -7.5°$

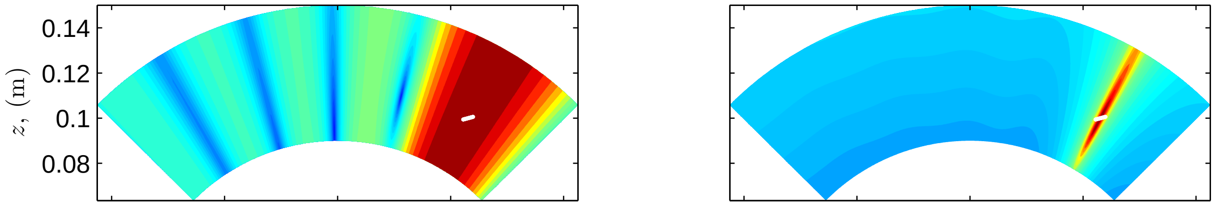

(c) $\alpha = 15°$

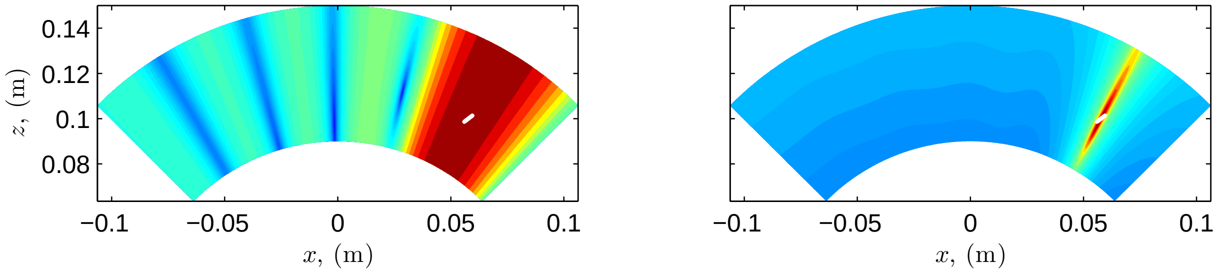

(d) $\alpha = 37.5°$

Figure 10: (left) DSBF, and (right) MUSIC for a crack versus varying crack orientation angles, α *(same color map as figure 9)*. Subfigures are organized counter–clock–wise for easy understanding. *(continued in the next page)*

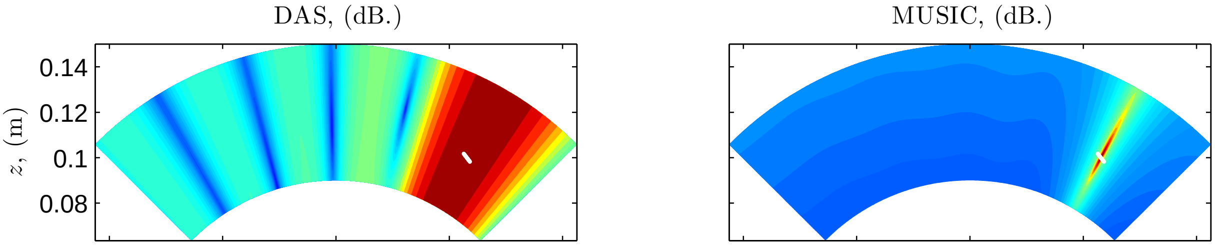

(h) $\alpha = 127.5°$

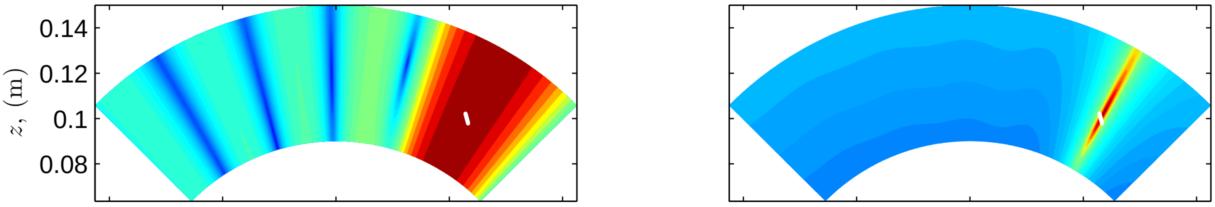

(g) $\alpha = 105°$

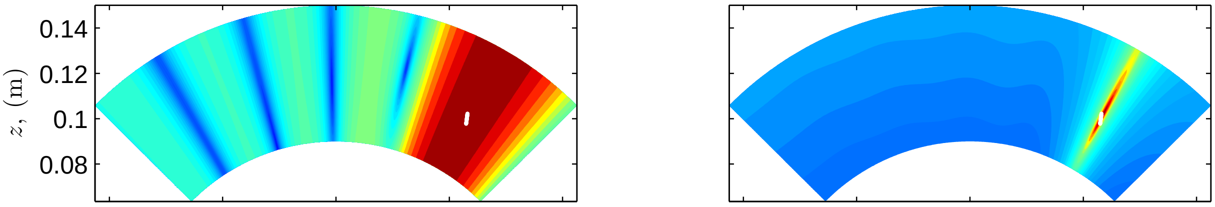

(f) $\alpha = 82.5°$

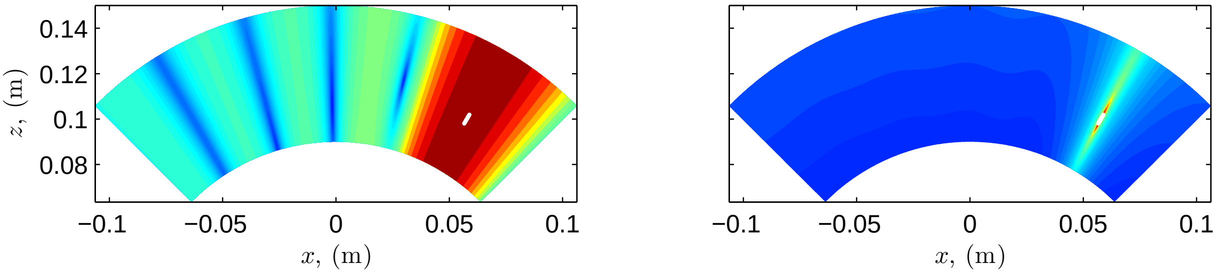

(e) $\alpha = 60°$ (coincident with the crack position vector)

Figure 10: *(continued)* (left) DSBF, and (right) MUSIC for a crack versus varying crack orientation angles, α *(same color map as figure 9)*. Subfigures are organized counter–clock–wise for easy understanding.

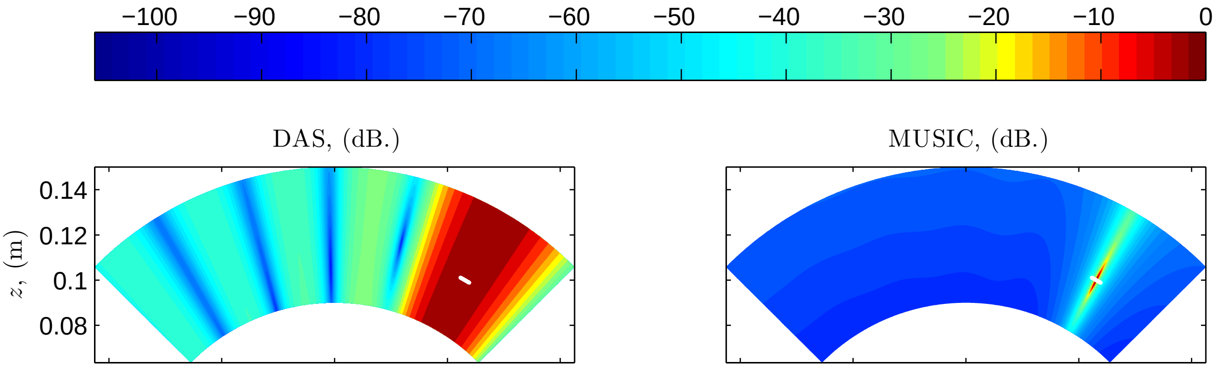

(a) 0.25λ; *identical to figure 9(b)*

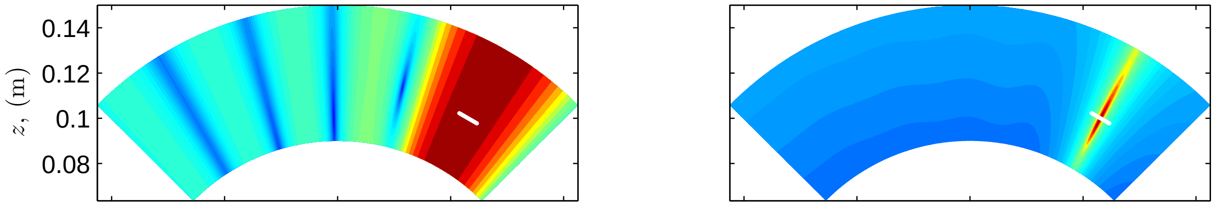

(b) 0.5λ

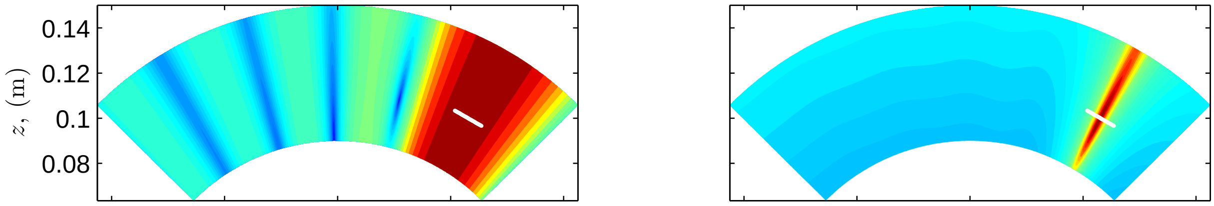

(c) 0.75λ

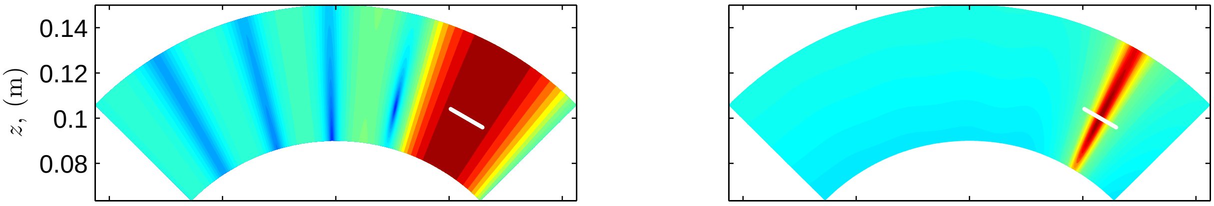

(d) 0.9λ

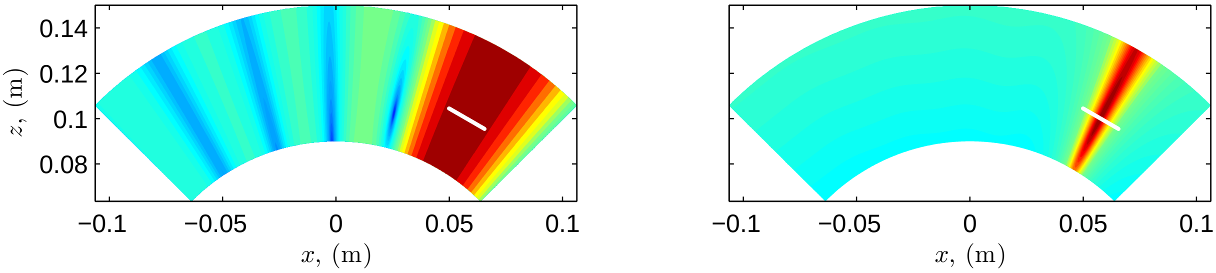

(e) λ

Figure 11: (left) DSBF, and (right) MUSIC for a crack located at $\theta = 60°$ and different crack lengths *(same color map as figure 9) (continued in the next page)*.

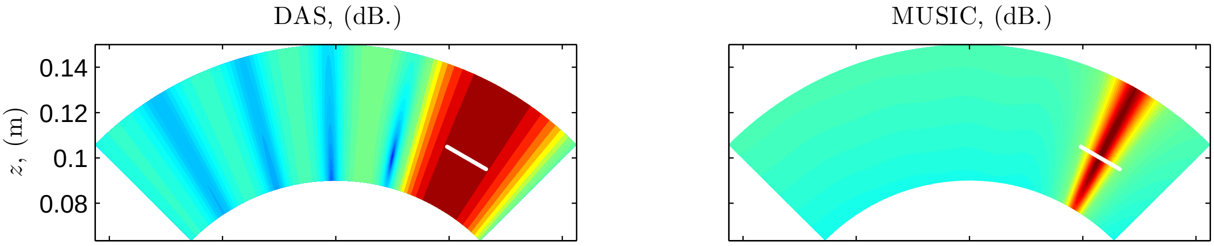

(f) 1.1λ

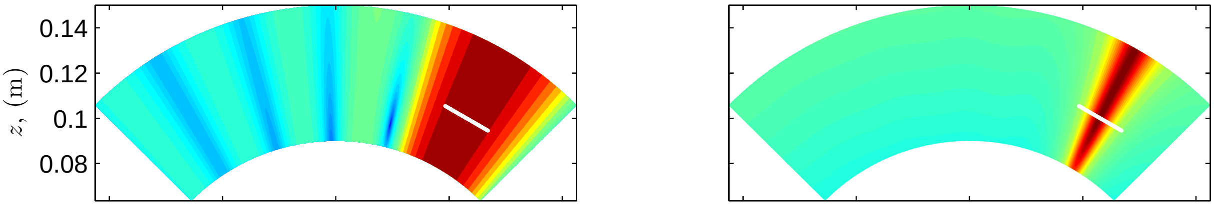

(g) 1.2λ

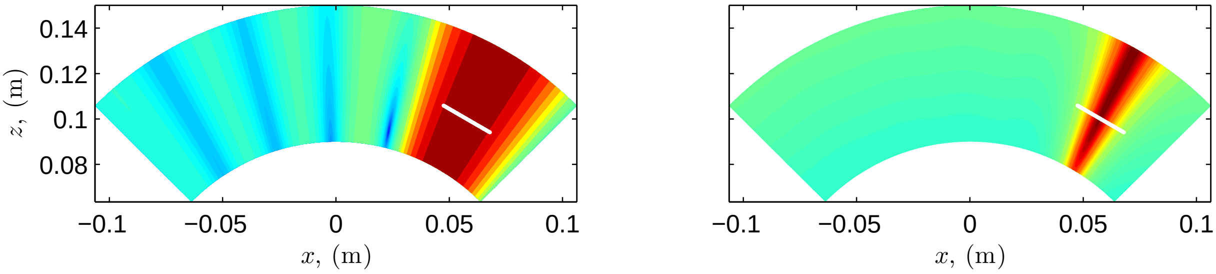

(h) 1.3λ

Figure 11: *(continued)* (left) DSBF, and (right) MUSIC for a crack located at $\theta = 60°$ and different crack lengths *(same color map as figure 9)*.

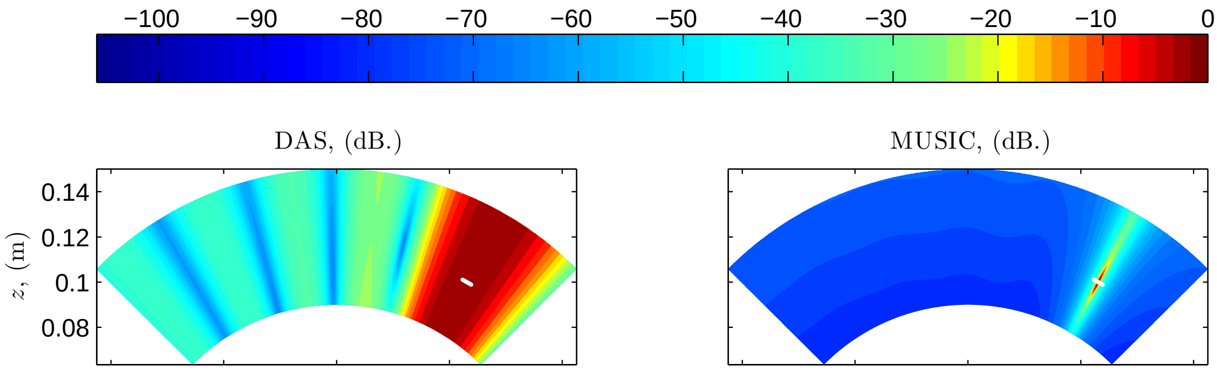

(a) SNR = 0.1

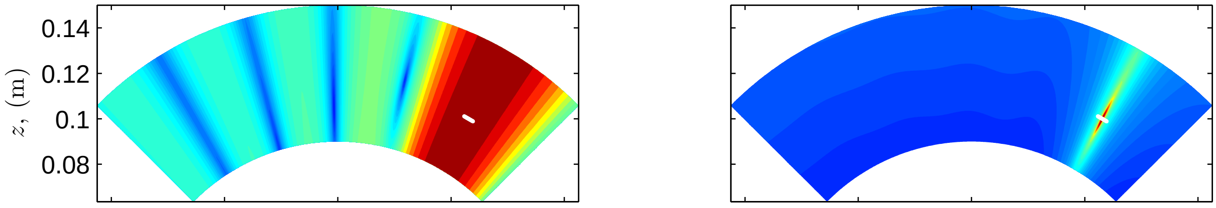

(b) SNR = 1; *identical to figure 9(b)*

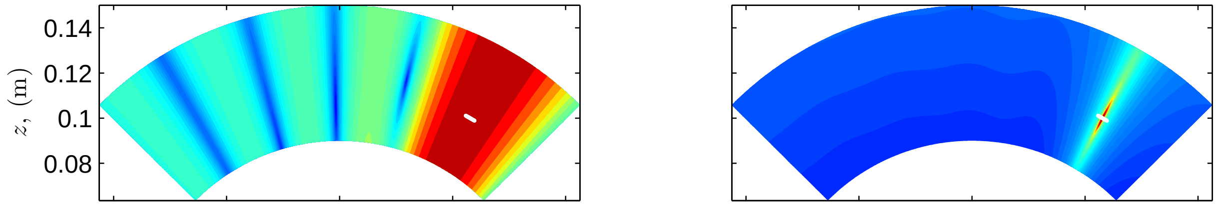

(c) SNR = 2

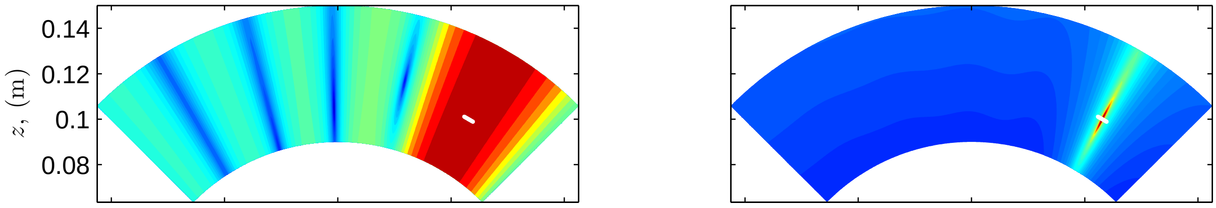

(d) SNR = 5

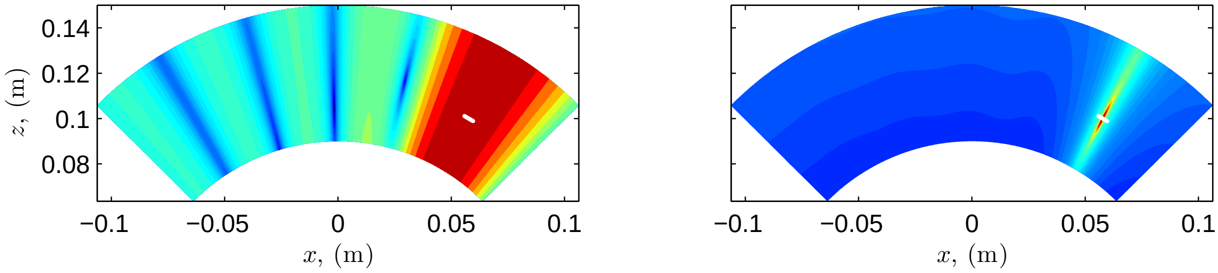

(e) SNR = ∞ (averaging is not useful for the deterministic excitation)

Figure 12: (left) DSBF and (right) MUSIC for a crack located at $\theta = 60°$, using **high** averaging, $N = 2048$ *(same color map as figure 9)*

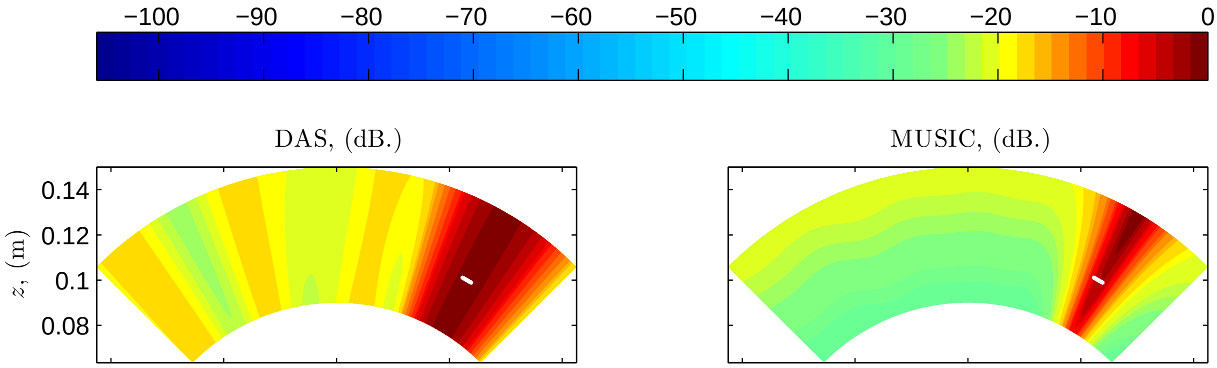

(a) SNR = 0.1

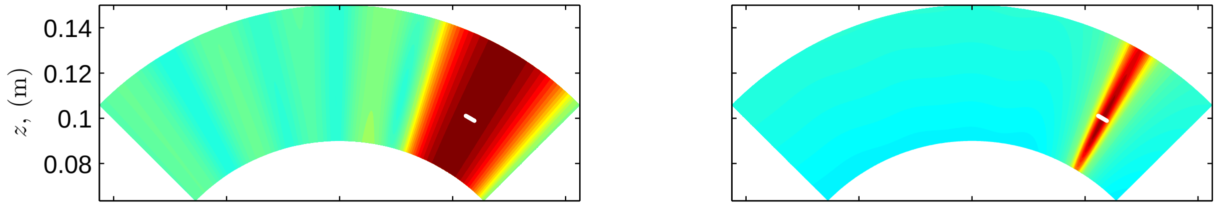

(b) SNR = 1

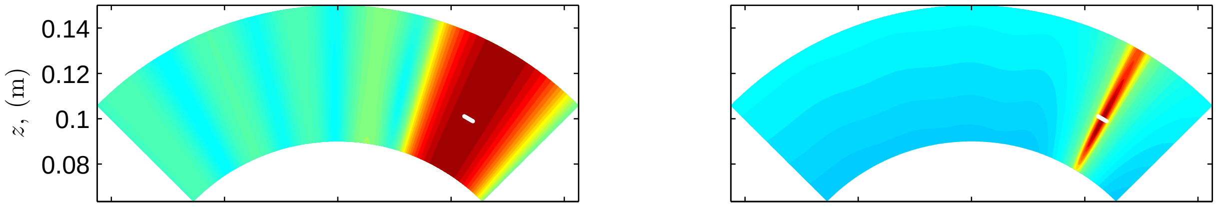

(c) SNR = 2

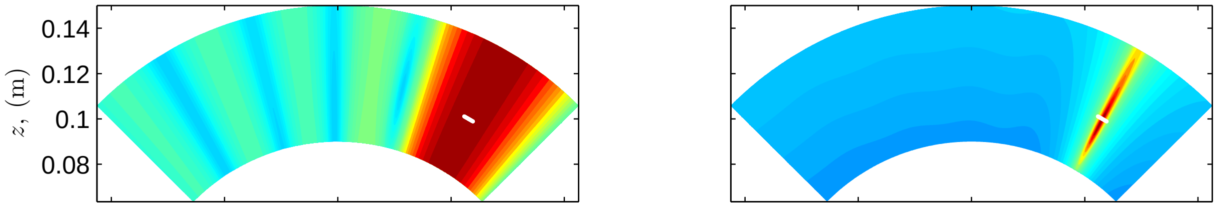

(d) SNR = 5

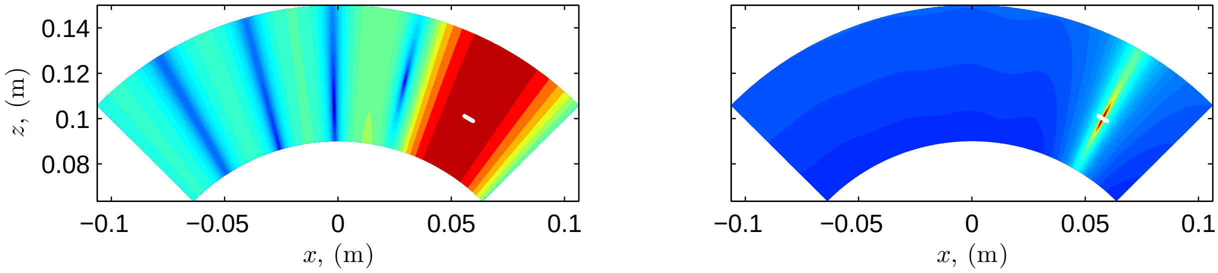

(e) SNR = ∞; *identical to figure 12(e)*

Figure 13: (left) DSBF and (right) MUSIC for a crack located at $\theta = 60°$, using **Low** averaging, $N = 16$ *(same color map as figure 9).*

6 Conclusion

This study comprehensively evaluated the performance of NF MUSIC algorithm for crack localization, by comparing it with the conventional DSBF method. The analysis examined several factors including crack angular position, orientation, size and SNR.

- Crack angular position:NF MUSIC accurately localizes cracks at arbitrary angles.
- Crack orientation: Resolution degrades as the crack deviates from orientations normal or parallel to the position vector.
- Crack size: While MUSIC correctly detects the range for sub-wavelength cracks, range resolution deteriorates for cracks exceeding the signal wavelength, though AOA resolution remains robust and linearly correlated with crack size.
- SNR: MUSIC exhibits strong noise resilience, maintaining high resolution even at low SNR levels when sufficient time averaging is applied. With reduced averaging, MUSIC still outperforms DSBF, though its range detection capability diminishes at very low SNR.

The results demonstrate that NF MUSIC achieves exceptional resolution in detecting both the AOA and range, whereas DSBF fails to resolve the range in all cases. These findings highlight MUSIC superiority in high–resolution defect localization, particularly in scenarios involving noise, arbitrary crack positions, and sub-wavelength defects. Future work could explore experimental validation under real–world conditions.

References

[1] A. Safari, “Improved defect characterisation using ultrasonic arrays,” Ph.D. dissertation, University of Bristol, 2020.

[2] G. Dobmann, D. Cioclov, and J. Kurz, “The role of probabilistic approaches in ndt defect-detection,-classification, and-sizing,” *Welding in the World*, vol. 51, no. 5, pp. 9–15, 2007.

[3] C. Wu, G. Xu, Y. Shan, X. Fan, X. Zhang, and Y. Liu, “Defect detection algorithm for wing skin with stiffener based on phased-array ultrasonic imaging,” *Sensors*, vol. 23, no. 13, p. 5788, 2023.

[4] O. Casula, C. Poidevin, G. Cattiaux, and G. Fleury, “A flexible phased array transducer for contact examination of components with complex geometry,” in *Proceedings of the 16th World Conference on Nondestructive Testing, Montreal, QC, Canada*, vol. 30. Citeseer, 2004.

[5] H. Hu, J. Du, C. Ye, and X. Li, “Ultrasonic phased array sparse-tfm imaging based on sparse array optimization and new edge-directed interpolation,” *Sensors*, vol. 18, no. 6, p. 1830, 2018.

[6] V. T. Prado, “Ultrasonic non–destructive testing of plate–like structures using piezoelectric array transducers,” phdthesis, 2014.

[7] A. Desoki, M. Mahgoub, and H. Negm, “Array signal processing for crack detection in plates,” in *Proceedings of the 17th International Conference on Applied Mechanics and Mechanical Engineering*, 2016, pp. MD–31 to MD–35.

[8] E. O. Brigham, *The fast Fourier transform and its applications.* Prentice–Hall, 1988.

[9] P. Stoica and R. Moses, *Spectral Analysis Of Signals.* Prentice Hall, 2005.

[10] V. S. U. Pillai, *Array signal processing.* New York: Springer Verlag, 1989.

[11] D. Johnson and D. Dudgeon, *Array Signal Processing: Concepts and Techniques*, ser. Prentice–Hall signal processing series. P T R Prentice Hall, 1993.

[12] L. Yu and V. Giurgiutiu, “In–situ optimized pwas phased arrays for Lamb waves structural health monitoring,” *Journal of mechanics of materials and structures*, vol. 2, no. 3, pp. 459–487, 2007.

[13] V. Giurgiutiu, *Structural health monitoring with piezoelectric wafer active sensors.* Burlington: Academic Press, 2007.

[14] J. S. Bendat and A. G. Piersol, *Random Data: Analysis and Measurement Procedures*, 1st ed. John Wiley & Sons, 2000.

[15] A. Desoki, J. ichi Takada, and I. Hagiwara, "Improved finite samples resampling for unbiased wide–band direction of arrival estimation," *Acoustical Science and Technology*, vol. 30, no. 6, pp. 417–428, 2009.